

RESEARCH

Open Access



Reduced graphene oxide/TiO₂/NiFe₂O₄ nanocomposite as a stable photocatalyst and strong antibacterial agent

Kamal Mohammed Jihad^{1,2}, Mahmood Rezaee Roknabadi^{1,2*} , Mojtaba Mohammadi¹ and Elaheh K. Goharshadi³

Abstract

In this study, we prepared reduced graphene oxide (rGO)/titanium dioxide (TiO₂)/nickel ferrite (NiFe₂O₄) nanocomposites with different mass ratios of rGO, TiO₂, and NiFe₂O₄ by a simple hydrothermal method. These nanocomposites were found to exhibit enhanced visible light harvesting, reduced electron–hole recombination, and improved magnetic properties compared to rGO, TiO₂, and NiFe₂O₄. The study evaluated the photocatalytic and antibacterial activity of the nanocomposites, with particular emphasis on the GTN211 (with a mass ratio of 2:1:1 for rGO:TiO₂:NiFe₂O₄) nanocomposite. The results showed that the GTN211 nanocomposite exhibited the best photocatalytic performance under both UV and visible light irradiation, achieving 95 and 89% degradation of Methylene Blue dye in 15 min, respectively. The study also investigated the photodegradation mechanism using various scavengers and found that holes were the main active species in the process. In addition to photocatalytic activity, the GTN211 nanocomposite also showed good antibacterial activity against *Escherichia coli* and *Staphylococcus aureus* bacteria, with the minimum inhibitory concentration of 1 mg mL⁻¹ for both bacteria and a minimum bactericidal concentration of 0.8 and 1 mg mL⁻¹, respectively. Hence, the GTN211 nanocomposite has potential as a material for environmental remediation and biomedical applications. The combination of photocatalytic and antibacterial activity makes this material a promising candidate for a wide range of applications.

Keywords rGo/TiO₂/NiFe₂O₄ nanocomposite, Methylene blue, Photocatalytic degradation, Antibacterial agent

1 Introduction

The rapid increase in population has made the removal of harmful organic compounds and dyes from the environment a significant challenge for both research and industry. To address this issue, many studies have investigated

the degradation of various pollutants, including dyes and bacteria, in water resources using nanomaterials [1]. Water resources are often contaminated with both organic and inorganic pollutants, as well as pathogenic agents [2].

Among nanomaterials used for wastewater treatment, TiO₂-based photocatalysts have gained widespread use due to their unique properties such as chemical stability, corrosion resistance, and non-toxicity [3]. TiO₂ nanoparticles (NPs) possess photocatalytic activity and antibacterial properties [4], making them an attractive option for wastewater treatment. The photocatalytic activity of TiO₂ arises from its superior photoactivation ability. The antimicrobial activity of TiO₂ is typically attributed to

*Correspondence:

Mahmood Rezaee Roknabadi
roknabad@um.ac.ir

¹ Department of Physics, Ferdowsi University of Mashhad, Mashhad 9177948974, Iran

² Angstrom Thin Film Research Laboratory, Ferdowsi University of Mashhad, Mashhad 9177948974, Iran

³ Department of Chemistry, Faculty of Science, Ferdowsi University of Mashhad, Mashhad 9177948974, Iran



© The Author(s) 2023. **Open Access** This article is licensed under a Creative Commons Attribution 4.0 International License, which permits use, sharing, adaptation, distribution and reproduction in any medium or format, as long as you give appropriate credit to the original author(s) and the source, provide a link to the Creative Commons licence, and indicate if changes were made. The images or other third party material in this article are included in the article's Creative Commons licence, unless indicated otherwise in a credit line to the material. If material is not included in the article's Creative Commons licence and your intended use is not permitted by statutory regulation or exceeds the permitted use, you will need to obtain permission directly from the copyright holder. To view a copy of this licence, visit <http://creativecommons.org/licenses/by/4.0/>.

the production of reactive oxygen species (ROS) under irradiation in the presence of oxygen. ROS affect bacterial cells through various mechanisms, leading to their death. In the absence of light, TiO_2 can also alter the permeability and shape of the bacterial cell wall, disrupting the osmotic balance of the bacteria [5]. However, the photocatalytic activity of TiO_2 is mostly limited to the UV region, and the electron-hole (e^-/h^+) recombination rate for this photocatalyst is high [6]. To overcome the limitations of TiO_2 , researchers have explored methods such as doping it with certain elements or combining it with other nanomaterials such as reduced graphene oxide (rGO) nanosheets and nickel ferrite (NiFe_2O_4). NiFe_2O_4 , in particular, is a promising magnetic material due to its many advantages, including stability, high electrical resistivity, high permeability, level of anisotropy, and simple preparation [7]. Its inverted spinel structure has Fe^{+3} metal ions occupying all tetrahedral sites and half of the octahedral sites, while Ni^{+2} occupies eight sites [8]. NiFe_2O_4 exhibits superparamagnetic behavior at the nanoscale and finds wide applications in magnetic fluids and drug delivery [9]. NiFe_2O_4 can also act as carriers for transferring antibacterial substances along with other nanostructures [10]. Although there have been relatively few studies on the use of NiFe_2O_4 for the elimination of organic pollutants through photocatalytic processes, some researchers have made significant progress in this area. Liang et al. [11] developed a photocatalyst of rGO-supported NiFe_2O_4 that exhibited superior photodegradation performance and recycling stability for the degradation of organic pollutants under visible-light irradiation. Gautam et al. [12] developed magnetic NiFe_2O_4 /graphene sand composite and NiFe_2O_4 /bentonite nanocomposites that achieved almost complete mineralization of ampicillin and oxytetracycline antibiotics under solar light.

To improve the photocatalytic property of NiFe_2O_4 , its composites with two-dimensional structure materials such as $g\text{-C}_3\text{N}_4$ or other photocatalytic semiconductors such as ZnO and TiO_2 were synthesized. For example, Hung and Thanh [13] prepared $\text{NiFe}_2\text{O}_4\text{-TiO}_2$ magnetic NPs that achieved 98.2% degradation of Methyl Orange dye after 14 h. Rahmayeni et al. [14] synthesized magnetic NPs of $\text{TiO}_{1.99}\text{NiFe}_2\text{O}_4$ that had higher photocatalytic activity than synthesized TiO_2 for the degradation of Rhodamine B under solar light irradiation. These results suggest that the synergistic effect of rGO, TiO_2 , and NiFe_2O_4 may enhance light absorption and improve their photocatalytic and antibacterial properties.

In our previous study, we investigated the photocatalytic property of rGO/ TiO_2 nanocomposites for degrading Methylene Blue (MB) under UV and visible light irradiation [15]. In this study, we prepared rGO/ TiO_2 /

NiFe_2O_4 (GTN) nanocomposites using a simple and scalable method to enhance interface effects and improve e^-/h^+ separation in rGO/ TiO_2 . Additionally, considering that rGO and TiO_2 can kill bacteria and cause cell membrane damage [16], suggesting that GTN nanocomposite may have potential as a photocatalyst with good antibacterial properties. The aims of this study are to investigate the photocatalytic property of GTN against MB under UV or visible light, as well as its antibacterial properties against *Staphylococcus aureus* and *Escherichia coli*.

2 Materials and methods

2.1 Materials

Titanium isopropoxide (TTIP, $\text{Ti}[\text{OCH}(\text{CH}_3)_2]_4$, 97%), nickel chloride (NiCl_2 , 98%), ferric chloride (FeCl_3 , 98%), silver nitrate (AgNO_3 , 99%), tert-butanol ($(\text{CH}_3)_3\text{COH}$, 99.5%), p-benzoquinone ($\text{C}_6\text{H}_4\text{O}_2$, 98%), potassium persulfate ($\text{K}_2\text{S}_2\text{O}_8$, 99%), ethylenediaminetetraacetic acid ($\text{C}_{10}\text{H}_{16}\text{N}_2\text{O}_8$, EDTA, 98%), dimethyl sulfoxide (DMSO, 99%), polyvinylpyrrolidone (PVP), potassium chloride (99%), potassium permanganate (KMnO_4 , 99%), graphite (99%), sodium iodide (99.9%), ammonia aqueous solution (NH_4OH , 28%), sodium hydroxide (NaOH , 97%), phosphoric acid (H_3PO_4 , 85%), hydrogen peroxide (H_2O_2 , 30%), and ethanol ($\text{C}_2\text{H}_5\text{OH}$, 99%) were provided from Sigma Aldrich (Merck, Burlington, MA, USA). Hydrochloric acid (HCl, 37%), sulfuric acid (H_2SO_4 , 49%), and nitric acid (HNO_3 , 65%) was purchased from Fluka. All chemicals in the present work were of analytical grade and used without further purification.

2.2 Preparation of graphite oxide (GtO)

GtO was synthesized using a modified Hummers method [15]. A total of 0.08 mol of graphite flakes were added to a 100 mL mixture of sulfuric acid, phosphoric acid, and nitric acid in a volumetric ratio of 67.5:10:22.5, respectively. The solution was then cooled in an ice bath while 0.04 mol of potassium permanganate was gradually added, ensuring that the temperature remained below 20 °C. The mixture was subsequently stirred for 2 h at a temperature range of 45–50 °C. After stirring, 100 mL of deionized (DI) water was added to the solution and agitated for 15 min while being maintained at a temperature of 85 °C for approximately 1 h. An additional 120 mL of DI water was then added, followed by the slow addition of 15 mL of hydrogen peroxide at a concentration of 30%, causing the solution to change color from dark brown to yellow.

To remove excess metal ions, the mixture was filtered and washed with a 1:10 hydrochloric acid aqueous solution (100 mL). The black unexfoliated precipitate was then separated by centrifugation at a speed of 750 rpm. Once the pH of the colloid reached 7, the remaining

yellow solution was centrifuged at a speed of 8000 rpm and the precipitate was washed several times with DI water. The resulting powder was left to dry at room temperature overnight.

2.3 Synthesis of TiO₂ NPs

TiO₂ NPs were synthesized using a sol gel method [15]. A total of 0.002 mol of TTIP and 0.4 mol of PVP were each dissolved in 50 mL of absolute ethanol. The two solutions were then combined and stirred for 10 min. Subsequently, a sodium hydroxide solution with a concentration of 1 M was gradually added to the mixture dropwise until the solution turned opaque. The resulting white powder was then separated by centrifugation, dried at a temperature of 50 °C, and calcined at a temperature of 400 °C for a duration of 2 h.

2.4 Synthesis of NiFe₂O₄ powder

NiFe₂O₄ NPs were synthesized using a hydrothermally assisted co-precipitation method [7]. Initially, a mixture of 0.02 mol of ferric chloride hexahydrate (FeCl₃·6H₂O), 0.01 mol of nickel chloride hexahydrate (NiCl₂·6H₂O), and 100 mL of deionized (DI) water was refluxed for 30 min at a temperature of 80 °C. Subsequently, 10 mL of

ammonium hydroxide was added to the reaction mixture and refluxed at a temperature of 80 °C for a duration of 3 h. The solution was then transferred to a stainless-steel autoclave and heated to a temperature of 180 °C for 8 h. The resulting powder was washed with ethanol and DI water before being dried in an oven at a temperature of 50 °C for a duration of 12 h.

2.5 Synthesis of GTN nanocomposites

The synthesis process of GTN nanocomposites is illustrated in Fig. 1. Initially, separate solutions of TiO₂, NiFe₂O₄, and GtO powders were prepared by dissolving each powder in 50 mL of DI using a sonicator operating at a frequency of 25 kHz. Subsequently, 0.03 mol of sodium hydroxide was dissolved in the dispersed TiO₂ solution. The resulting solution, along with the NiFe₂O₄ solution, was then added dropwise to the dispersed graphene oxide (GO) suspension. A 200 mL homemade, Teflon-lined, stainless-steel autoclave was filled with 150 mL of the final solution and heated to a temperature of 100 °C for a duration of 18 h. The resulting powder was separated using a magnet and washed with DI water until the pH reached 7 before being left to dry at room temperature. Four nanocomposites were

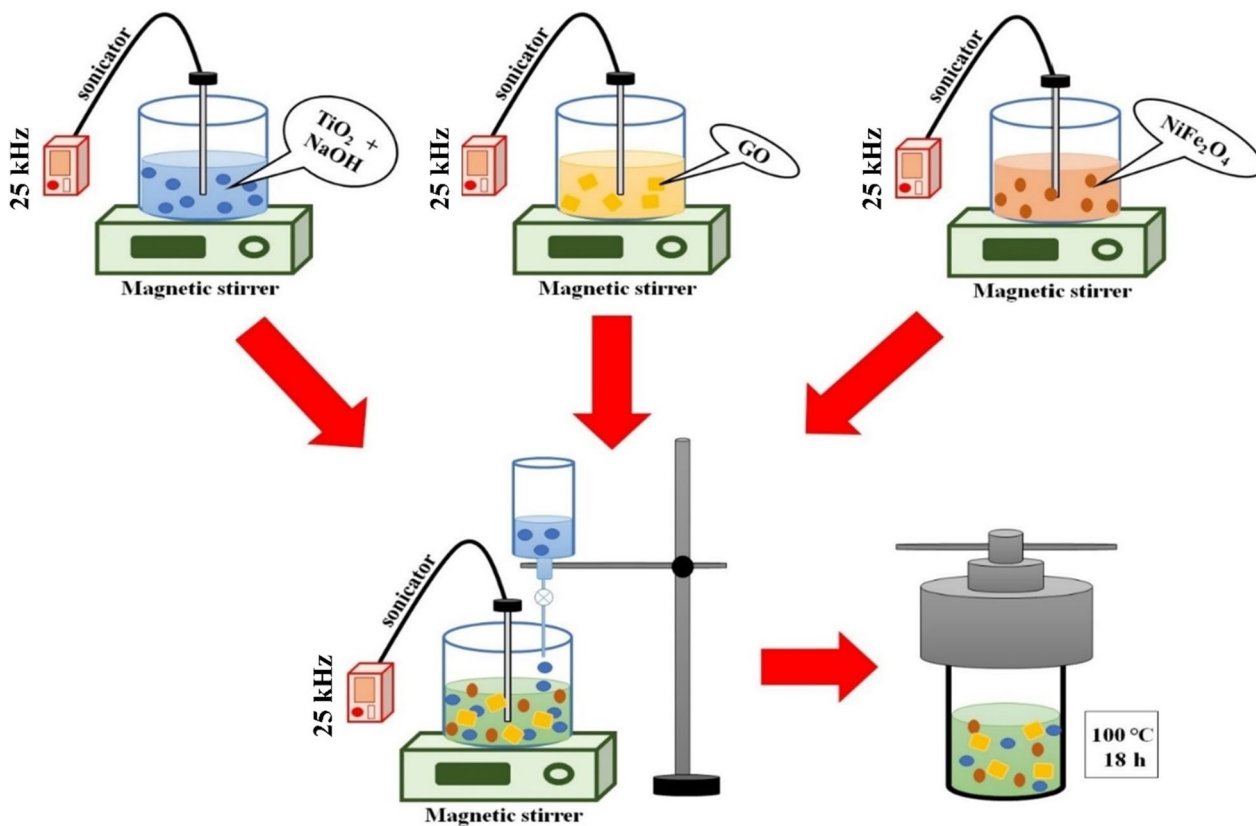


Fig. 1 Schematic of the rGO/TiO₂/NiFe₂O₄ nanocomposites synthetic process

synthesized using this method with the mass ratio of $\text{TiO}_2\text{:NiFe}_2\text{O}_4$ being fixed at 1:1 for all samples. The mass ratio of $\text{rGO-TiO}_2\text{-NiFe}_2\text{O}_4$ (GTN) was varied as 1:1:1, 2:1:1, 3:1:1, and 4:1:1 and the resulting nanocomposites were named GTN111, GTN211, GTN311, and GTN411, respectively.

2.6 Photocatalytic experiments

To evaluate the photocatalytic activity of the synthesized materials, we conducted experiments by dispersing 5 mg of each photocatalyst in 50 mL of DI water containing 20 ppm of MB. The resulting solution was stirred in the dark for 30 min at 25 °C to establish an equilibrium between adsorption and desorption. After this dark conditioning step, the solution was exposed to a UV or visible (Xenon lamp, 700 W) lights for 105 min to initiate the photocatalytic reaction. The light source was positioned at a fixed distance from the solution and provided a consistent irradiance throughout the duration of the experiment. During the exposure period, we periodically collected samples from the solution and measured the absorbance of MB at the wavelength of 664 nm using a UV-Vis spectrophotometer. These experiments allowed us to evaluate the efficiency of the photocatalysts in degrading MB under light irradiation and to compare their photocatalytic performance. The results provide insight into the potential applications of these materials in various fields, including wastewater treatment and pollution remediation. Two different light sources of 500 W Osram Xenon lamp equipped with a UV cutoff filter at 400 nm, serving as a visible light source with an intensity of 50 mW cm^{-2} , and a 200 W HBO Mercury short arc lamp, serving as a UV light source with an intensity of 50 mW cm^{-2} were used. During each experiment, 5 mL of the solution was extracted at specific time intervals and the photocatalyst was separated using a magnet. The absorbance of the filtered supernatant was measured using a UV-Vis spectrophotometer at the maximum wavelength, λ_{max} , of MB, which is 665 nm.

To identify the active species responsible for the photodegradation of MB by GTN211 under visible light irradiation, different radical scavengers were employed at a concentration of 3 mM. These scavengers included p-benzoquinone (PBQ, 98%) for superoxide radical ion, silver nitrate (AgNO_3 , 99%) and potassium persulfate ($\text{K}_2\text{S}_2\text{O}_8$, 99%) as electron scavengers, sodium azide (NaN_3 , 99.5%) for singlet oxygen, DMSO (99%) for bulk hydroxyl radicals ($^{\bullet}\text{OH}_{\text{bulk}}$), tert-butanol (t-BuOH, 99.5%) for free hydroxyl radicals ($^{\bullet}\text{OH}$), sodium iodide (NaI, 99.9%) for adsorbed hydroxyl radicals ($^{\bullet}\text{OH}_{\text{ads}}$), and ethylenediaminetetraacetic acid (EDTA, 98%) as a hole scavenger.

2.7 Antibacterial activity measurements

The antibacterial activity of GTN211 was evaluated using microbroth dilution methods in a 96-well microtiter plate against Gram-negative (*E. coli* ATCC 25922) and Gram-positive (*S. aureus* ATCC 25923) bacteria [17]. The choice of GTN211 tested for antibacterial activity was made to capture the overall trends of the nanocomposites' performance and to provide a representative demonstration of their potential as novel photocatalysts and strong antibacterial agents. We believe that the results obtained from this sample are indicative of the broader behavior within the series and contribute significantly to the understanding of the GTN nanocomposites' antibacterial properties.

Bacterial cells were cultivated in nutrient broth medium, consisting of 13 g of nutrient broth dissolved in 1 L of DI water and sterilized at a temperature of 121 °C. The bacteria were grown in the nutrient broth medium (NBM) while shaking at a speed of 150 rpm for a duration of 18 h at a temperature of 37 °C. Bacterial growth was then controlled to achieve a standard turbidity at a wavelength of 630 nm, corresponding to a concentration of $1.5 \times 10^8 \text{ CFU mL}^{-1}$. The nanocomposite was prepared at different concentrations (4, 2, 1, 0.8, 0.6, 0.4, 0.2, 0.1, and 0.05 mg mL^{-1}) in DI water and sterilized in an autoclave at a temperature of 121 °C for 20 min. The nanocomposite was then dispersed using an ultrasonic bath operating at a frequency of 60 Hz for 30 min prior to the experiments. A volume of 10 μL of each bacterial strain was added to each well of the microtiter plate containing 100 μL of nutrient broth with varying concentrations of the nanocomposite. Wells containing different concentrations of the nanocomposite suspensions in nutrient broth without bacterial inoculum, wells containing bacterial inoculum with nutrient broth without nanocomposite, and wells containing only nutrient broth were used as blank, positive, and negative controls, respectively.

The microplates were incubated at a temperature of 37 °C and after a duration of 18 h, the optical density was measured at a wavelength of 600 nm using an ELIZA microplate reader ELX800 (BioTeck, USA). The percentage of bacterial survival was calculated using Eq. (1):

$$\text{Bacteria survival (\%)} = \frac{T - (B + P)}{P - N} \times 100 \quad (1)$$

where B represents the blank well and T, N, and P represent the absorbance values for the test, negative control, and positive control wells, respectively.

The minimum bactericidal concentration (MBC) is the lowest concentration of the antibacterial agent that can kill bacteria and prevent any further bacterial growth on nutrient agar plates [18]. To prepare the nutrient agar medium (37 g L^{-1}), 20 mL of sterilized medium was

added to petri dishes and allowed to solidify. The MBC value was determined by subculturing 10 μL of each sample onto nutrient agar plates and incubating them for 18 h at 37 °C. After incubation, the plates were examined for bacterial growth, and the MBC was recorded as the lowest concentration of the nanocomposite that showed no bacterial growth. This method allowed us to determine the efficacy of the nanocomposites in inhibiting bacterial growth and provided valuable information on their potential as antibacterial agents.

2.8 Instruments

The phase purity of the synthesized nanocomposites was analyzed using an X-ray diffraction (XRD) instrument (D8 Advance Bruker YT model, CuKα radiation). The crystallite size of NPs was calculated using the Debye–Scherrer formula, which is defined as follows:

$$D = \frac{k\lambda}{\beta \cos \theta} \tag{2}$$

where D is the crystallite size, k is the shape factor, λ is the X-ray wavelength, β is the line broadening at half maximum intensity in radians and θ is the Bragg angle.

The atomic force microscopy (AFM) was performed using a Full 0101-Ara Research Company model. We utilized the TESCAN-XMU instrument equipped with the Quantax 200 EDX detector from Bruker to acquire field emission scanning electron microscopy (FE-SEM) images and perform elemental mapping of the samples. Transmission electron microscopy (TEM) images were obtained using a Leo 912AB system. UV–Vis spectroscopy data were recorded using a UVD2950 system. The band gap (E_g) values of the nanocomposites were calculated using the following equation [19]:

$$E_g = \frac{1240}{\lambda} \tag{3}$$

where λ represents the wavelength and E_g is the band gap in eV. The value 1240 is a conversion factor that allows the units of wavelength (nm) to be canceled out, resulting in a final value for E_g in eV. This conversion factor is derived from the relationship between energy (E), wavelength, and Planck’s constant (h) in the equation $E = hc/\lambda$, where c is the speed of light. By expressing h in eV s and the speed of light in nm s⁻¹, the value of hc becomes 1240 eV nm, allowing the units of wavelength (nm) to be canceled out when calculating E_g . The magnetic properties of the synthesized nanocomposites were investigated at ambient temperature using a vibrating sample magnetometer (VSM, Lake Shore Cryotronics 7407 model). Fourier transform infrared spectroscopy (FTIR) data were obtained using an AVATAR-370 Thermo Nicolet FTIR spectrometer. The pH of the solution was measured using a pH meter (Model 86,502, AZ).

3 Results and discussion

3.1 Characterization of prepared nanomaterials

AFM is a powerful tool for studying the surface morphology and topography of nanomaterials. Figure 2 shows the AFM image of two-dimensional structure of GO. The thickness of the GO sheets can be determined from the height measurements in the AFM images, which are typically on the order of nanometers. In this case, the thickness of the GO sheets is approximately 1.5 to 3.0 nm, indicating that they are composed of a few atomic layers and are thin-layered. The AFM image also reveals the surface roughness and defects of the GO sheets. The surface roughness arises from the presence of the oxygen functional groups, which introduce height variations on

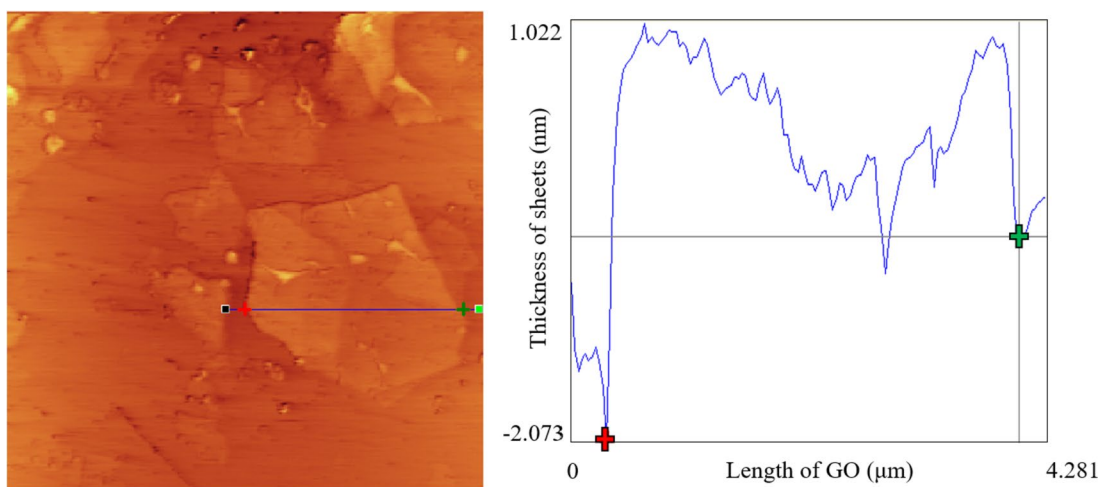


Fig. 2 AFM image of prepared GO sheets

the basal plane of graphene. The defects, such as wrinkles, folds, and tears, are common in thin-layered materials due to their high flexibility and susceptibility to mechanical stress.

XRD is a widely used technique for studying the crystal structure and phase composition of materials. The XRD patterns for TiO₂, NiFe₂O₄, and GO are presented in Fig. 3a–c, respectively. Using Eq. (2), the crystallite size was calculated for the (101) plane of the TiO₂ and the (311) plane of NiFe₂O₄ NPs which was 25 and 13 nm, respectively. The TiO₂ sample showed XRD peaks at 2θ = 25.3, 37.8, 48.1, 54.1, 62.4, 68.7, 70.6, and 74.9°. These peaks correspond to the (101), (004), (200), (105), (204), (116), (220), and (215) planes of anatase TiO₂ (JCPDS-No.21–1272) with a tetragonal crystal system and preferred orientation along (101) plane [15]. The XRD pattern of NiFe₂O₄ exhibited peaks at 2θ of 18.4, 30.3, 35.6, 43.3, 53.7, 57.4, 63.0, 71.5, and 74.8°. These peaks correspond to the (111), (220), (311), (400), (422), (511), (440), (620), and (533) planes of spinel phase

NiFe₂O₄ with a cubic crystal system and space group Fd-3m (JCPDS Card No.10–0325). The preferred orientation for this sample is the (311) plane [20, 21]. For GO, only a single XRD peak was observed at 2θ = 11° corresponding to its (001) plane oxide [15]. Using Eq. (2), the crystallite size for TiO₂ and NiFe₂O₄ was calculated to be 25 and 13 nm, respectively. Figure 3d shows the XRD pattern of the prepared nanocomposites, which provides important information on the structural properties of the materials. The XRD pattern reveals the presence of diffraction peaks for both TiO₂ and NiFe₂O₄ NPs, which confirms their crystalline structure in the nanocomposites. Furthermore, the XRD pattern also indicates that TiO₂ and NiFe₂O₄ NPs have been successfully loaded onto the surface of rGO nanosheets. This is evident from the appearance of diffraction peaks that correspond to both the NPs and the rGO nanosheets. The diffraction peaks for the rGO nanosheets are broad and weak, which is typical of amorphous carbon materials. The successful loading of TiO₂ and NiFe₂O₄ NPs onto the rGO

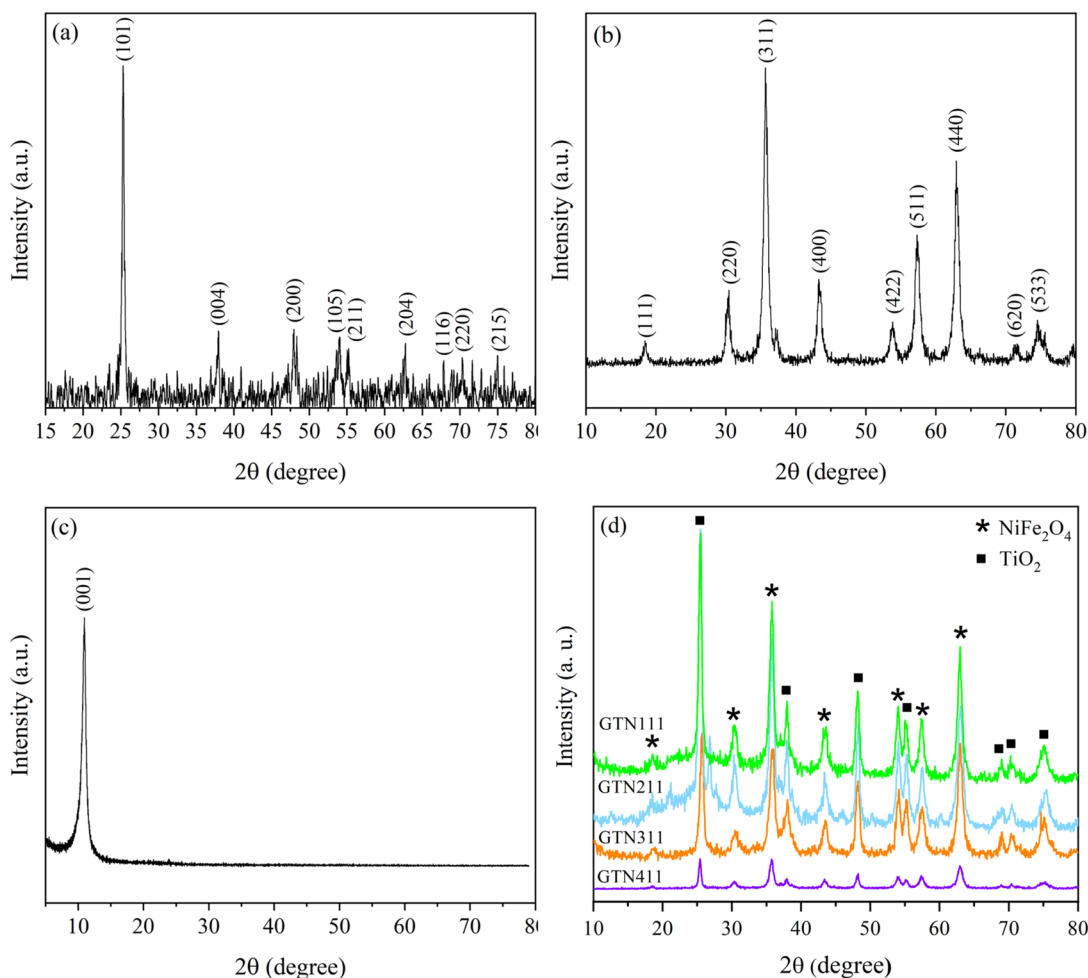


Fig. 3 The XRD patterns of (a) TiO₂ (b) NiFe₂O₄ (c) GO and (d) nanocomposites

nanosheets is important for enhancing their properties and potential applications. The rGO nanosheets provide a high surface area and good electrical conductivity, which can improve the performance of the nanocomposites in various applications such as photocatalysis, energy storage, and sensing.

TEM is a powerful technique for studying the morphology and structure of nanomaterials. In Fig. 4, the TEM images of GO sheets, TiO₂, and NiFe₂O₄ provide valuable insights into the morphology and structure of the individual components of the prepared nanocomposites. The TEM micrograph of GO (Fig. 4a) shows the wrinkled and folded nature of the GO sheets, which is consistent with the AFM images in Fig. 2. The wrinkles and folds arise from the presence of oxygen functional groups on the basal plane of graphene, which introduce height variations and distortions in the planar structure. The TEM images of the TiO₂ (Fig. 4b) reveal the presence of tetragonal cubic nanocrystals, which is consistent with the XRD results in Fig. 3d. The size of the TiO₂ NPs

is larger than the NiFe₂O₄ NPs, which is also consistent with the XRD results. The larger size of the TiO₂ NPs can be attributed to the higher crystallinity and growth rate of the tetragonal anatase phase. As seen in Fig. 4c, the TEM image of NiFe₂O₄ NPs shows that the particles have an almost cubic shape, which is consistent with the crystal structure of NiFe₂O₄. The particles appear to be well-defined and uniform in size, indicating a good dispersion on the surface of rGO nanosheets.

Figure 5a presents the UV–Vis absorption spectra of various nanocomposites and GO. GO exhibits a distinct peak at 230 nm, which is attributed to the π–π* transition of C=C bonds, as well as a shoulder at 300 nm that corresponds to the π–π* transition of C=O bonds [22]. A notable blue shift in the absorption edge is observed for the samples in comparison to GO, indicating an increase in visible light harvesting by the nanocomposites [23]. This suggests that the nanocomposites are active photocatalysts under visible light. Further analysis of Fig. 5a reveals that the absorption edges of GTN111, GTN211,

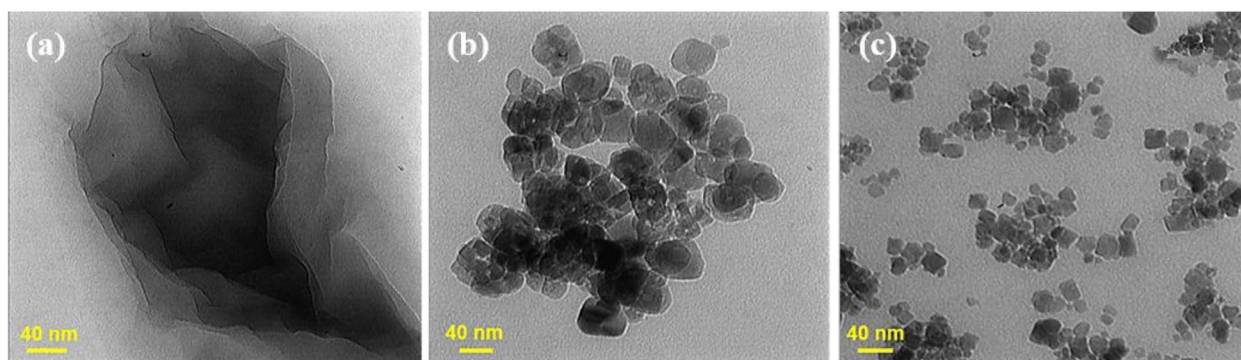


Fig. 4 The TEM images of (a) GO, (b) TiO₂, and (c) NiFe₂O₄

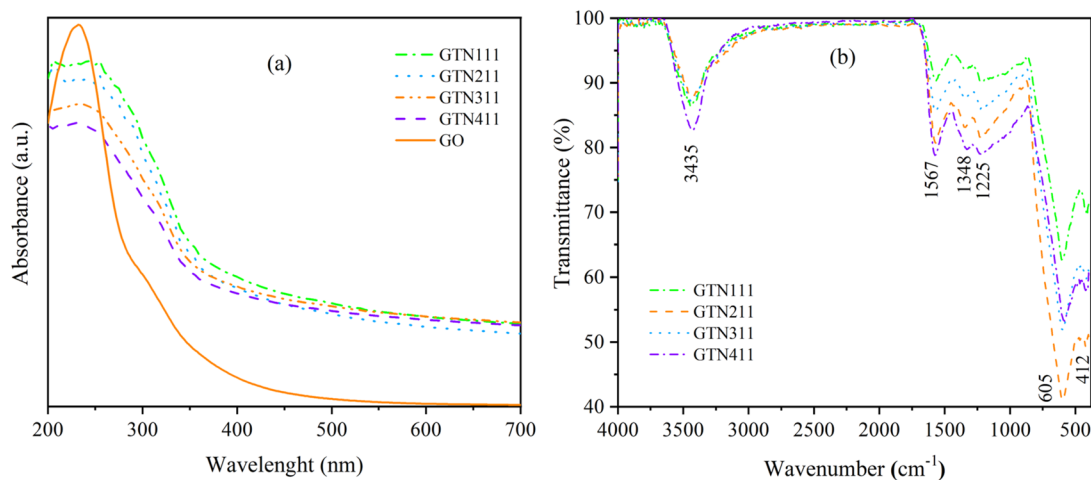


Fig. 5 a UV–Vis absorption spectra and (b) FTIR spectra of nanocomposites

GTN311, GTN411, and GO are 475, 469, 442, 431, and 319 nm, respectively. The calculated band gap values for GTN111, GTN211, GTN311, GTN411, and GO according to Eq. (3) are 2.61, 2.64, 2.81, 2.88, and 3.89 eV, respectively. This indicates that GTN111 and GTN211 have the lowest band gaps and are thus capable of harvesting more visible light compared to the other samples.

The FTIR spectrum for the GTN is presented in Fig. 5b, which displays several characteristic bands. The Fe–O stretching vibration at wavenumber of 605 cm^{-1} is one of the most prominent bands in the FTIR spectrum of the GTN nanocomposite [24, 25]. The metal–oxygen bond is formed by the electrostatic attraction between the positively charged metal cation and the negatively charged oxygen atoms. The band observed at 1378 cm^{-1} corresponds to the $-\text{CH}_2$ group [26], which is a characteristic vibration of organic compounds containing a methylene ($-\text{CH}_2$) group. This band can be used to identify and characterize the presence of organic compounds in the samples. The $-\text{CH}_2$ group is a common functional group found in a wide range of organic compounds, such as alkanes, alkenes, and alkynes. The presence of the $-\text{CH}_2$ peak in the FTIR spectrum of the sample suggests the presence of organic compounds in these materials. Another prominent band observed in the FTIR spectrum is the broad band at approximately 3435 cm^{-1} , which is associated with the stretching vibration of the hydroxyl ($-\text{OH}$) functional group present in water [26]. The presence of this band indicates that water molecules are present in the samples. Water is a ubiquitous molecule that can be present in a wide range of materials and environments. In the case of the GTN nanocomposites, the presence of water molecules could be due to the synthetic process or could be absorbed from the surrounding environment during storage or handling. The C–OH and C=C stretching modes are assigned to the bands at 1225 and 1567 cm^{-1} , respectively [27–29]. The presence of these bands suggests that the samples may contain organic compounds or functionalized carbon materials, such as rGO. The C=C stretching mode, on the other hand, is a characteristic feature of aromatic compounds containing a carbon–carbon double bond. The presence of the C=C band indicates that the samples may contain aromatic compounds or functionalized carbon materials, such as GO or rGO.

Figure 6 depicts SEM images of the synthesized nanocomposites at two different magnifications, revealing differences in their surface morphology and particle size. The SEM images show that the GTN111 and GTN211 have smoother, more regular, and uniform surfaces than the other nanocomposites, with particles arranged in an orderly manner and of similar sizes. However, the GTN211 has smaller and more uniform particles than

the GTN111, as indicated by the scale in the image. In contrast, the GTN311 has a more regular and uniform surface compared to the GTN411 sample. However, the GTN411 sample has a rougher surface with particles of varying sizes, likely due to the presence of impurities or agglomeration during synthesis. It is worth noting that the size and morphology of the particles can significantly influence the properties and performance of the nanocomposites in various applications. For instance, smaller and more uniform particles can provide a larger surface area and better dispersion, leading to improved catalytic activity, sensing, and energy storage. All nanocomposites demonstrate that the surface of GO is completely covered with titanium dioxide and nickel ferrite NPs. Also, Fig. 6 shows the elemental mappings of the synthesized nanocomposites, which provide a visual representation of the spatial distribution and relative abundance of different elements. The mappings reveal a heterogeneous structure with different regions enriched in various elements. To investigate the elemental composition and distribution in detail, we employed EDX spectroscopy and elemental mapping. Figure 7 displays the EDX spectra of the nanocomposites, exhibiting characteristic peaks corresponding to different elements. We summarized the W% (The weight percentage and A% (The atomic percentage)) of each element in each sample in Table 1. The results of the elemental analysis indicate that as the mass ratio of rGO to TiO_2 and NiFe_2O_4 increases from GTN111 to GTN411, there is a corresponding increase in the weight and atomic percentages of carbon and a decrease in the weight and atomic percentages of Ti, Fe, and Ni. Moreover, the elemental analysis shows that the nanocomposites have relatively low Fe and Ni contents, suggesting that most of the metal NPs are encapsulated by carbonaceous materials.

It is worth mentioning that to calculate the weight percentage of an element in a sample, we divided the mass of that element by the total mass of the sample. In the case of the GTN111, GTN311, and GTN411, the total mass of each sample is determined by the sum of the masses of rGO, TiO_2 , and NiFe_2O_4 . While the mass of rGO varies among these samples, with GTN111 having the lowest mass and GTN411 having the highest mass, the masses of TiO_2 and NiFe_2O_4 are constant between all three samples. As a result, the total mass of each sample increases as the mass of rGO increases from GTN111, GTN311, and to GTN411. However, changes in the total mass of a sample can affect the weight percentage of each element, even if the mass of that element remains constant. For instance, as the total mass of a sample increases due to an increase in the mass of rGO, the weight percentages of other elements such as carbon and oxygen can change even if their masses remain constant.

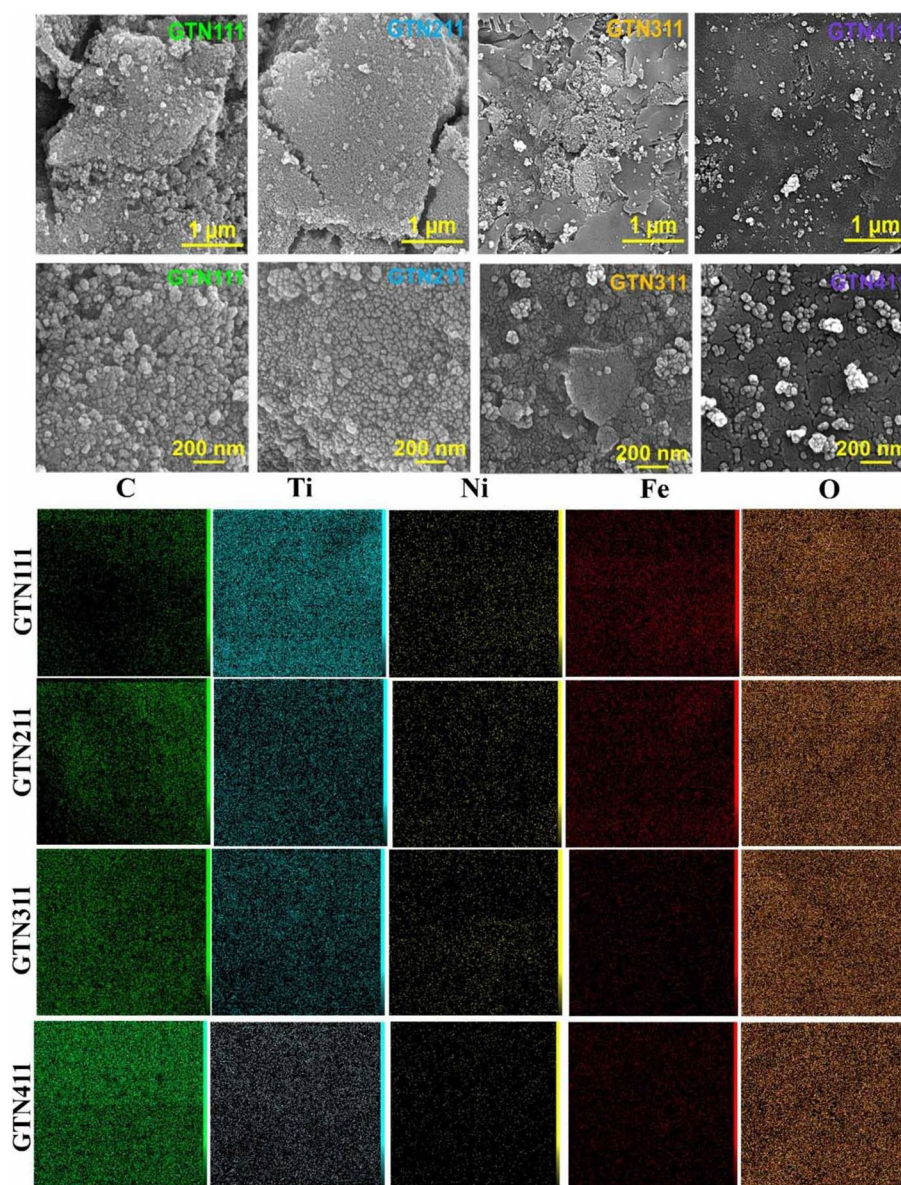


Fig. 6 FE-SEM images and the corresponding elemental mappings of synthesized nanocomposites

In the case of carbon, the weight percentage may only increase slightly in GTN411 compared to GTN311, even though the concentration of rGO is different by one-fold between these two samples. This is because the increase in total mass of GTN411 due to its higher rGO content can result in a smaller increase in its weight percentage of carbon compared to what would be expected based on its higher carbon content alone. Similarly, in the case of oxygen its weight percentage may be lower in GTN411 compared to GTN111, even though its rGO content has been quadrupled. This is because the increase in total mass of GTN411 due to its higher rGO content can result

in a decrease in its weight percentage of oxygen if its oxygen content remains constant. Additionally, other factors such as variations in sample preparation or measurement error could contribute to differences in weight percentages between these samples.

Figure 8 represents the hysteresis curves of all samples at room temperature. Table 2 shows the magnetic properties of the synthesized nanocomposites, including the saturation magnetization (M_s), coercivity (H_c), and remanence magnetization (M_r). The M_s value indicates the maximum induced magnetic moment that can be obtained in a magnetic field, beyond this field

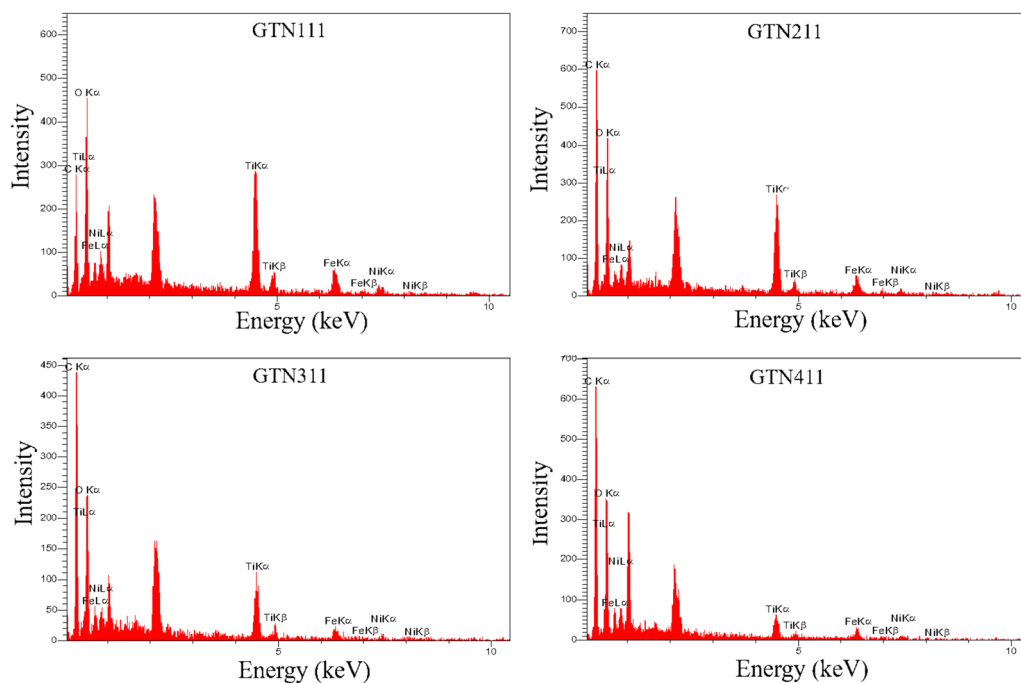


Fig. 7 The EDX spectra of nanocomposites

Table 1 EDX analysis results of nanocomposites

Sample	Element									
	C		O		Ti		Fe		Ni	
	W (%)	A (%)	W (%)	A (%)	W (%)	A (%)	W (%)	A (%)	W (%)	A (%)
GTN111	25.7	38.5	45.7	51.4	17.8	6.7	7.3	2.3	3.6	1.1
GTN211	41.7	55.3	38.5	38.4	13.2	4.4	5.3	1.5	1.4	0.4
GTN311	47.1	58.6	40.5	40.5	8.1	2.5	2.7	0.7	1.5	0.4
GTN411	51.0	61.0	40.9	36.78	3.4	1.0	2.9	0.8	1.7	0.4

no further increase in magnetization occurs. The H_c value represents the intensity of the applied magnetic field required to reduce the magnetization of the material to zero after the magnetization of the sample has been driven to saturation. The M_r value indicates the magnetization left behind in a ferromagnetic material after an external magnetic field is removed. All these data can be extracted from Fig. 8. The $NiFe_2O_4$ has the highest M_s value of 53 emu g^{-1} , indicating that it has the strongest magnetization among all samples. The GTN111 has the second highest M_s value of 19 emu g^{-1} , followed by the GTN211, GTN311, and GTN411 with 17, 13, and 11 emu g^{-1} , respectively. Interestingly, the addition of GO and TiO_2 reduces the magnetization of the nanocomposites. The H_c values of the samples range from 1.6 to 3.2 Oe, with the GTN211 having the

highest H_c value and the $NiFe_2O_4$ having the lowest H_c value. This implies that the GTN211 is the most resistant to demagnetization, while the $NiFe_2O_4$ is the least resistant. The M_r values of the samples range from 0.14 to 0.34 emu g^{-1} , with the GTN211 having the highest M_r value and the $NiFe_2O_4$ having the lowest M_r value. This indicates that the GTN211 retains the most magnetization after removing an external magnetic field, while the $NiFe_2O_4$ retains the least. Based on Table 2, it can be concluded that the GTN211 has the best overall magnetic performance among all samples, with high M_s , H_c , and M_r values. In contrast, the $NiFe_2O_4$ has the worst magnetic performance, despite having the highest M_s value. Other nanocomposites show intermediate magnetic properties, demonstrating the influence of the composition and structure on the magnetic behavior.

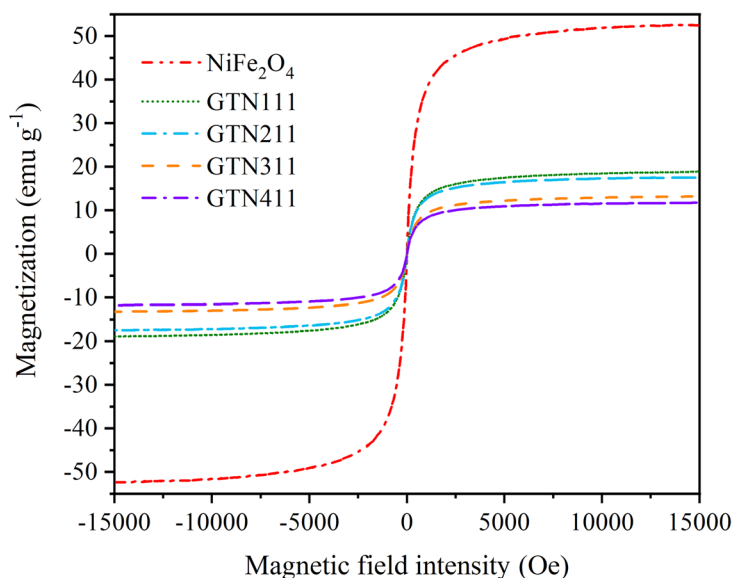


Fig. 8 The hysteresis curve of the pure NiFe₂O₄ and nanocomposites

Table 2 Saturation magnetization (M_s), Coercivity (H_c), and magnetic remanence (M_r) of samples

Sample	M_s (emu g ⁻¹)	H_c (Oe)	M_r (emu g ⁻¹)
NiFe ₂ O ₄	53	1.6	0.14
GTN111	19	2.9	0.33
GTN211	17	3.2	0.34
GTN311	13	2.1	0.28
GTN411	11	2.7	0.30

3.2 Photodegradation of MB

The photocatalytic performance of different photocatalysts for degrading MB under UV and visible lights irradiation for 105 min was evaluated by the ratio of C/C_0 (where C_0 and C are the initial and the time-dependent dye concentrations, respectively) and presented in Fig. 9a and b, respectively. Prior to irradiation, the MB solution containing the photocatalysts was kept in the dark for 30 min to reach the adsorption–desorption equilibrium.

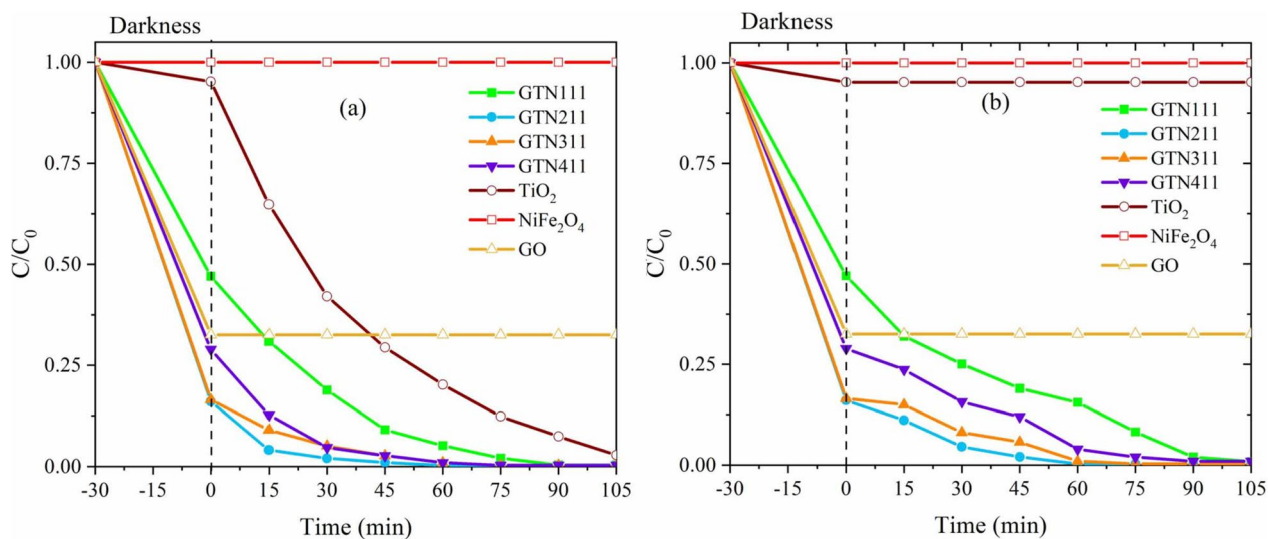


Fig. 9 The photocatalytic activity of prepared photocatalysts against MB dye (a) under UV light and (b) under visible light irradiation. Experiments used 5 mg photocatalyst in 50 mL DI water with 20 ppm MB, stirred in dark for 30 min before 105 min light exposure

During this period, the adsorption process was completed. Upon exposure to UV and visible lights, the dye degradation was initiated. As depicted in Fig. 9, the nanocomposites exhibit superior photocatalytic activity compared to other photocatalysts. The most efficient degradation of MB under both UV and visible lights is achieved by GTN211 (about 95 and 89% under UV and visible lights for 15 min, respectively). The results show that GTN211 is a superior photocatalyst for degrading MB dye under both UV and visible lights, compared to other materials such as $\text{Co}_{0.5}\text{Zn}_{0.25}\text{Ni}_{0.25}\text{Fe}_2\text{O}_4\text{-TiO}_2$, $\text{Co}_{0.5}\text{Zn}_{0.25}\text{Mn}_{0.25}\text{Fe}_2\text{O}_4\text{-TiO}_2$ [30] and $\text{ZnO/TiO}_2/\text{rGO}$ [31]. GTN211 nanocomposite can achieve a high dye degradation efficiency (95 and 89% under UV and visible lights, respectively) in a short time (15 min), while the other materials require longer irradiation time (80 min for $\text{Co}_{0.5}\text{Zn}_{0.25}\text{Ni}_{0.25}\text{Fe}_2\text{O}_4\text{-TiO}_2$, $\text{Co}_{0.5}\text{Zn}_{0.25}\text{Mn}_{0.25}\text{Fe}_2\text{O}_4\text{-TiO}_2$) or have lower dye degradation efficiency (43 and 41% for $\text{ZnO/TiO}_2/\text{rGO}$ at pH 9 and 7, respectively) under the same conditions. The superior photocatalytic performance of GTN211 nanocomposite can be attributed to the presence of rGO, which can enhance the visible light harvesting, reduce the e^-/h^+ recombination, and improve the adsorption of dye molecules on the surface of the photocatalyst, as well as TiO_2 and NiFe_2O_4 NPs, which can generate ROS under light irradiation and oxidize the dye molecules. In addition, GTN211 nanocomposite can achieve higher dye degradation efficiency than $\text{ZnO/TiO}_2/\text{rGO}$ nanocomposite at different pH values, which indicate that GTN211 nanocomposite is more versatile and adaptable than $\text{ZnO/TiO}_2/\text{rGO}$ nanocomposite for different water conditions. In general, the following reasons cause this increase in MB degradation in GTN nanocomposites:

- (1) The harvesting visible light for all nanocomposites is better than that of other prepared photocatalysts prepared in this work.
- (2) The π - π interaction between the conjugated structure of rGO and benzene rings of MB improves the dye adsorption further on the surface of the nanocomposites.
- (3) Due to embedding of TiO_2 NPs on the surface of rGO, e^-/h^+ recombination decreases [15, 32].

The photocatalytic degradation of MB by TiO_2 NPs and all nanocomposites under visible light obeyed the pseudo-first-order kinetics [32, 33], as represented by Eq. (4).

$$-\ln(C/\text{CO}) = kt \quad (4)$$

where k is the pseudo-first-order kinetic constant (min^{-1}). The pseudo-first-order kinetic model for degradation of

Table 3 The pseudo-first-order kinetic constant of photocatalysts for the degradation of MB (0.1 mg mL⁻¹ of photocatalyst, 20 ppm of MB, 50 mW cm⁻² intensity of light, 25°C)

Sample	k_1 (min^{-1})			
	UV light	R ²	Visible light	R ²
TiO_2	0.031	0.97	0	--
GTN111	0.053	0.96	0.0365	0.95
GTN211	0.050	0.98	0.0621	0.98
GTN311	0.052	0.99	0.0593	0.97
GTN411	0.057	0.99	0.0441	0.96

MB dye by prepared photocatalysts under both UV and visible light irradiation is shown in Table 3. The table presents the results of experiments using a pseudo-first-order kinetic model, with 0.1 mg mL⁻¹ of photocatalyst, 20 ppm of MB, 50 mW cm⁻² intensity of light, and at 25°C. The results demonstrate the effectiveness of the photocatalysts in degrading MB dye under both UV and visible light irradiation. Also, Table 3 presents the results of the degradation of MB using different photocatalysts. The highest the pseudo-first-order kinetic constant, k_1 , value under UV light irradiation is observed for the GTN411, with a value of 0.06 min⁻¹, indicating that GTN411 is the most efficient photocatalyst for MB degradation under UV light compared to all other samples. On the other hand, the highest k_1 value under visible light irradiation is observed for the GTN211 sample, with a value of 0.06 min⁻¹, indicating that GTN211 is the most efficient photocatalyst for MB degradation under visible light among all samples tested. In general, GTN411 is a good overall choice for photocatalytic degradation of MB as it exhibits high performance under both UV and visible light. It has the highest k_1 value under UV light and a relatively high k_1 value under visible light, indicating its efficiency in degrading MB under both types of irradiations. However, if the performance under visible light is more important, then GTN211 would be a better choice due to its highest k_1 value under visible light irradiation.

The cycling photocatalytic performance of the GTN211 sample was evaluated under both UV and visible light irradiation. To evaluate the cycling photocatalytic performance of the GTN211, tests were conducted under both UV and visible light irradiation, with three repetitions for accuracy and consistency. To reuse the photocatalyst, it was washed with DI water and dried in an oven. Then, the next experiment was performed. Figure 10 shows the cycling photocatalytic performance of GTN211 under both UV and visible light irradiation. The figure presents the results of experiments, demonstrating the stability and effectiveness of GTN211 as a photocatalyst under repeated cycles of irradiation. The

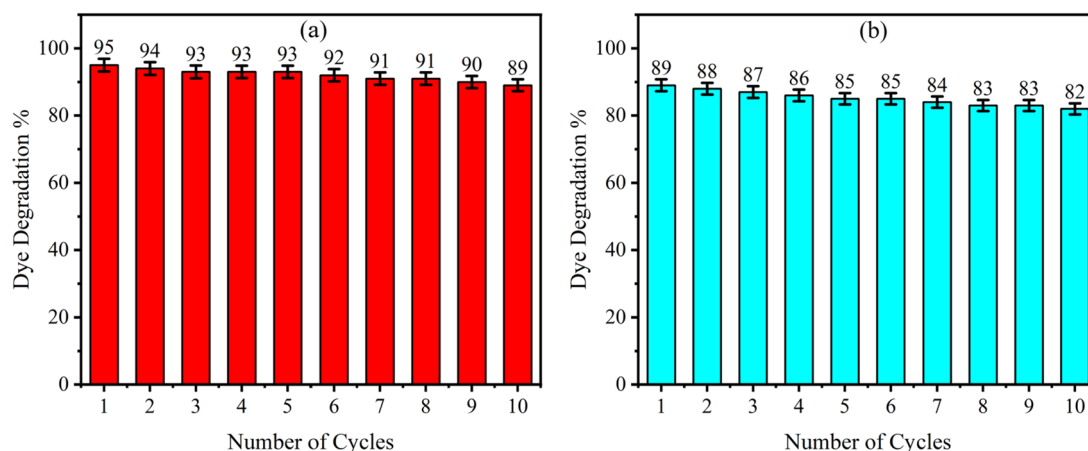


Fig. 10 The cycling photocatalytic performance of GTN211 under (a) UV and (b) visible light irradiation, respectively

Table 4 The cycling photocatalytic performance and standard deviation (SD) of GTN211 under UV and visible light irradiation

UV light			Visible light		
Number of cycles	Dye degradation (%)	SD	Number of cycles	Dye degradation (%)	SD
1	95	1.9	1	89	1.8
2	94	1.9	2	88	1.8
3	93	1.9	3	87	1.7
4	93	1.9	4	86	1.7
5	93	1.9	5	85	1.7
6	92	1.8	6	85	1.7
7	91	1.8	7	84	1.7
8	91	1.8	8	83	1.7
9	90	1.8	9	83	1.7
10	89	1.8	10	82	1.6

results are presented in Table 4, which shows that the sample achieved a higher dye degradation percentage under UV light compared to visible light for all cycles. In the first cycle, the dye degradation percentage was 95% under UV light and 89% under visible light. These values decreased to 89% and 82%, respectively, by the 10th cycle. The dye degradation percentage gradually decreased over the course of 10 cycles for both UV and visible light, with a slightly higher rate of decrease observed under visible light. The standard deviation values also decreased gradually over the number of cycles, from 1.9 to 1.8 for UV light and from 1.8 to 1.6 for visible light, indicating increased consistency in the results. Based on the results, it can be inferred that the GTN211 exhibits more effective photocatalytic activity under UV light than visible light. Although the dye degradation percentage decreased gradually over

the course of cycles, this decline was more prominent under visible light.

The photodegradation mechanism of MB by GTN211 under visible light was investigated using various scavengers with the same concentration of 3 mM. The scavengers were p-benzoquinone for superoxide radical ion, AgNO₃ and K₂S₂O₈ for electrons, NaN₃ for singlet oxygen, DMSO for [•]OH_{bulk}, tert-butanol for free OH radical, NaI for [•]OH_{ads}, and EDTA for holes [15, 34, 35]. The presence of the suitable scavenger would slow down or inhibit the photodegradation of MB by the photocatalyst if the corresponding reactive species was involved in the reaction [15, 36].

The experimental results, presented in Fig. 11 and obtained from three repetitions, indicate that MB is a photostable dye and did not undergo any degradation under light irradiation in the absence of the photocatalyst. However, in the presence of GTN211 and in the absence of any scavenger, the highest percentage of dye degradation was observed, with a 98% degradation of the dye after 60 min. The addition of AgNO₃, K₂S₂O₈, p-benzoquinone, and sodium azide did not significantly affect the photodegradation process, as the dye degradation percentages after 60 min were 95, 96, 95, and 90%, respectively. This suggests that electrons, superoxide radicals, or singlet molecular oxygen are not the primary active species in MB photodegradation. In contrast, the addition of EDTA significantly reduced the degradation efficiency of MB by GTN211, with a dye degradation percentage of only 23% after 60 min. This finding suggests that holes are the main active species throughout the photocatalytic degradation process and that EDTA is the strongest scavenger among those tested. Moreover, the addition of NaI, tert-butanol, and DMSO decreased the efficiency of photocatalytic degradation, with dye

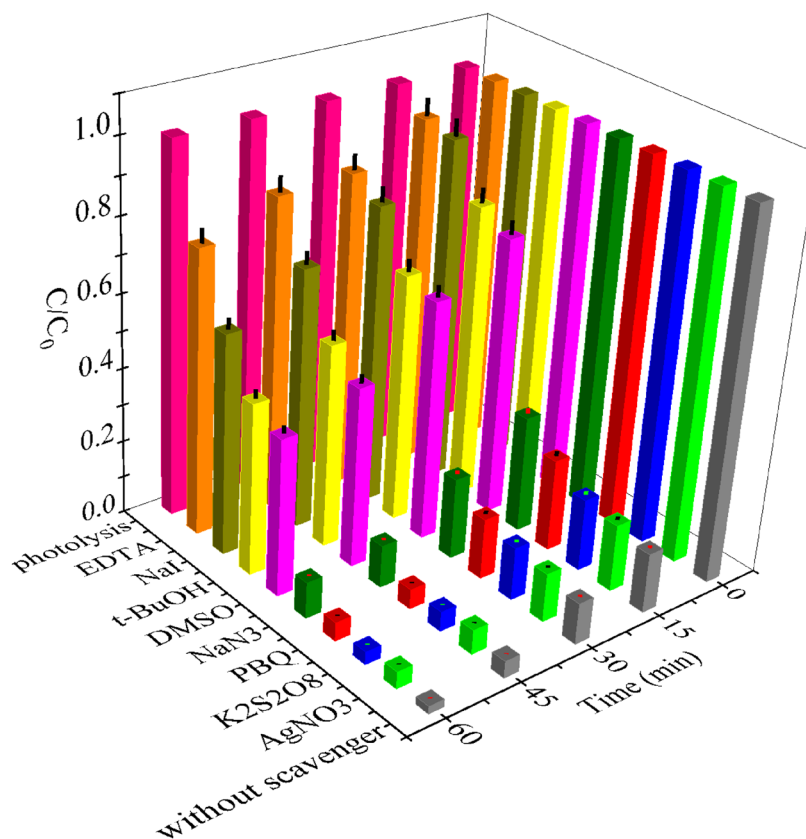


Fig. 11 Influence of several radical scavengers (AgNO₃, K₂S₂O₈, PBQ, NaN₃, DMSO, t-BuOH, NaI and EDTA) on the photodegradation of MB by GTN211 under visible light irradiation. The concentration of MB was maintained at 20 ppm

degradation percentages after 60 min of 40, 53, and 57%, respectively. This indicates that free and $\cdot\text{OH}_{\text{bulk}}$ play a supporting role in the process and that these scavengers had a moderate effect on the photodegradation efficiency. Hence, the results suggest that holes are the strongest oxidant species in MB photodegradation by GTN211 under visible light irradiation.

3.3 Antibacterial activity

The antibacterial properties of GTN211 nanocomposite were tested against *E. coli* and *S. aureus* bacteria, based on its effective photocatalytic capability. GTN211 showed a good antimicrobial activity, with the same MIC value of 1 mg mL⁻¹ for both bacteria. The MBC values were 0.8 and 1 mg mL⁻¹ for *E. coli* and *S. aureus*, respectively (Fig. 12). These results indicate that GTN211 has a bactericidal effect on both Gram-negative and Gram-positive bacteria, which could be attributed to the synergistic effect of rGO, TiO₂, and NiFe₂O₄ NPs in generating ROS and disrupting the bacterial membrane. In our previous work [16], we compared the antimicrobial activity of the nanocomposites of GO with TiO₂ with different mass ratios of TiO₂ and GO (2:1, 1:1, 1:2, and 1:4), named

as T2G1, T1G1, T1G2, and T1G4, respectively. We found that T2G1 had the highest antibacterial properties among nanocomposites, because the GO sheets in the sample enhanced the surface area for bacterial inactivation. The bacterial membranes were destroyed by the interaction with T2G1. In this work, GTN with the mass ratio of 2:1:1 had similar properties to T2G1. GTN211 was more effective against *E. coli* than *S. aureus*. The antibacterial activity of GTN211 was comparable to that of rGO/TiO₂/PVA composite, which showed a similar bacteria removal percentage of 78% against *E. coli* [37]. This implies that the polymer matrix (PVA) did not affect the antibacterial activity of rGO/TiO₂ NPs, but rather improved their stability and dispersion. Some other studies have also reported the antibacterial properties of rGO against *E. coli* and *S. aureus*. For example, Mann et al. [38] investigated the antibacterial activity of RGO against *E. coli* and found that RGO exhibited concentration-dependent effects. At high concentrations (200 and 400 μg mL⁻¹), RGO showed antibacterial activity, while at low concentrations (10 and 50 μg mL⁻¹), RGO showed no antibacterial effect but rather enhanced the bacterial growth. They suggested that RGO might interact with the bacterial

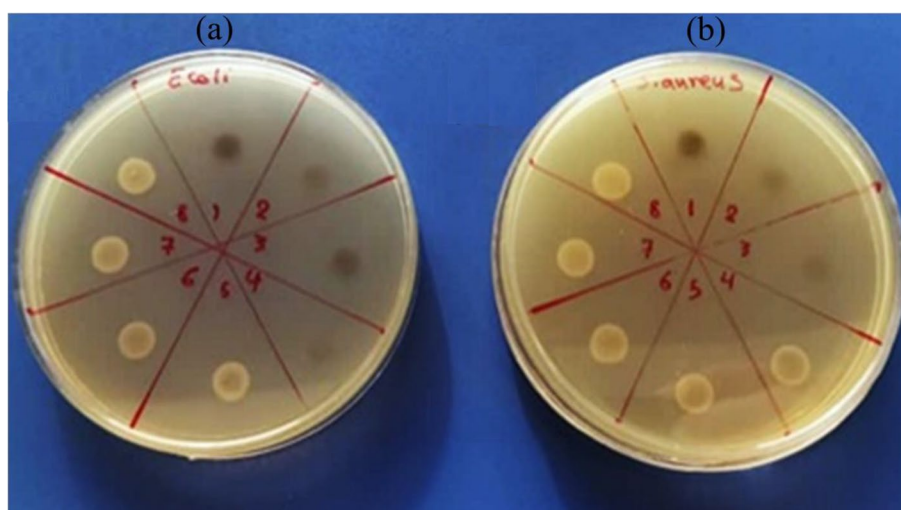


Fig. 12 MIC test of GTN211 nanocomposite for (a) *E. coli* and (b) *S. aureus* bacteria

cells and provide carbon source for their growth, as evidenced by X-ray photoelectron spectroscopy analysis. Therefore, the antibacterial activity of GTN211 can be further improved by modifying its structure or composition. For example, adding a shell layer of rGO or another metal oxide could enhance its ROS generation and membrane disruption ability, as demonstrated by $\text{NiFe}_2\text{O}_4@\text{TiO}_2/\text{rGO}$ nanocomposite [39]. Alternatively, changing the polymer matrix or the mass ratio of rGO, TiO_2 , and NiFe_2O_4 could affect its surface area, porosity, stability, and interaction with bacteria, as shown by $\text{rGO}/\text{TiO}_2/\text{PVA}$ and $\text{rGO}/\text{TiO}_2/\text{PEG}$ composites [37].

4 Conclusions

Using a simple hydrothermal method, we successfully synthesized GTN nanocomposites with varying mass ratios of rGO, TiO_2 , and NiFe_2O_4 . The nanocomposites were characterized using various techniques, and their photocatalytic and antibacterial properties were evaluated. Our results showed that the GTN nanocomposites exhibited superior properties compared to their pure components, including enhanced visible light harvesting, reduced e^-/h^+ recombination, improved magnetic properties, high photocatalytic efficiency, and good antibacterial activity. Among the nanocomposites, GTN211 exhibited the best performance under both UV and visible light irradiation, achieving 95 and 89% degradation of MB in 15 min, respectively. The photodegradation mechanism was dominated by holes as the main active species. Additionally, the GTN211 nanocomposite demonstrated good antibacterial activity against both *E. coli* and *S. aureus* bacteria, with a microbial inhibition concentration of 1 mg mL^{-1} and MIC of 0.8 and 1 mg mL^{-1} , respectively. Overall, our findings suggest that

the GTN211 nanocomposite is a promising material for environmental remediation and biomedical applications. Future work will focus on optimizing the synthesis conditions, exploring other applications, and investigating the stability and toxicity of the nanocomposites.

Acknowledgements

The support of Ferdowsi University of Mashhad (Grant no. 3/ 56995) Iran for this work is appreciated.

Authors' contributions

Kamal Mohammed Jihad analyzed the data, discussed the results, and writing-original draft preparation. Mahmood Rezaee Roknabadi; project administration, acquisition of funding, provided conceptualization, discussed the results and final proofed the manuscript. Mojtaba Mohammadi; provided conceptualization and contributed to the final version of the manuscript. Elaheh K. Goharshadi; provided conceptualization discussed the results and final proofed the manuscript. All authors have read and agreed to the published version of the manuscript.

Availability of data and materials

All data generated or analyzed during this study will be made available upon request.

Declarations

Competing interests

The authors declare that they have no known competing financial interests or personal relationships that could have appeared to influence the work reported in this paper.

Received: 28 April 2023 Accepted: 30 October 2023

Published online: 08 December 2023

References

1. Sajjadi SH, Goharshadi EK. Highly monodispersed hematite cubes for removal of ionic dyes. *J Environ Chem Eng.* 2017;5:1096–106.
2. Zare EN, Fallah Z, Le VT, Doan VD, Mudhoo A, Joo SW, et al. Remediation of pharmaceuticals from contaminated water by molecularly imprinted polymers: a review. *Environ Chem Lett.* 2022;20:2629–64.

3. Niazi Z, Goharshadi EK, Mashreghi M, Jorabchi MN. Highly efficient solar photocatalytic degradation of a textile dye by TiO₂/graphene quantum dots nanocomposite. *Photoch Photobio Sci*. 2021;20:87–99.
4. Sukhadeve GK, Bandewar H, Janbandhu SY, Jayaramaiah JR, Gedam RS. Photocatalytic hydrogen production, dye degradation, and antimicrobial activity by Ag-Fe co-doped TiO₂ nanoparticles. *J Mol Liq*. 2023;369:120948.
5. Li H, Wu J, Gao X, Li T, Zhang M, Niu X, et al. Preparation and performance study of antibacterial materials based on GO – TiO₂. *ChemistrySelect*. 2021;6:7880–6.
6. Ikram M, Hassan J, Raza A, Haider A, Naz S, Ul-Hamid A, et al. Photocatalytic and bactericidal properties and molecular docking analysis of TiO₂ nanoparticles conjugated with Zr for environmental remediation. *RSC Adv*. 2020;10:30007–24.
7. Malik AR, Aziz MH, Atif M, Irshad MS, Ullah H, Gia TN, et al. Lime peel extract induced NiFe₂O₄ NPs: Synthesis to applications and oxidative stress mechanism for anticancer, antibiotic activity. *J Saudi Chem Soc*. 2022;26:101422.
8. Alamier WM, Hasan N, Nawaz MDS, Ismail KS, Shkir M, Malik MA, et al. Biosynthesis of NiFe₂O₄ nanoparticles using *Murayya koenigii* for photocatalytic dye degradation and antibacterial application. *J Mater Sci Technol*. 2023;22:1331–48.
9. Irfan M, Dogan N, Bingolbali A, Aliew F. Synthesis and characterization of NiFe₂O₄ magnetic nanoparticles with different coating materials for magnetic particle imaging (MPI). *J Magn Magn Mater*. 2021;537:168150.
10. Bhosale SV, Ekambe PS, Bhoraskar SV, Mathe VL. Effect of surface properties of NiFe₂O₄ nanoparticles synthesized by dc thermal plasma route on antimicrobial activity. *Appl Surf Sci*. 2018;441:724–33.
11. Liang J, Wei Y, Zhang J, Yao Y, He G, Tang B, et al. Scalable green method to fabricate magnetically separable NiFe₂O₄-reduced graphene oxide nanocomposites with enhanced photocatalytic performance driven by visible light. *Ind Eng Chem Res*. 2018;57:4311–9.
12. Gautam S, Shandilya P, Singh VP, Raizada P, Singh P. Solar photocatalytic mineralization of antibiotics using magnetically separable NiFe₂O₄ supported onto graphene sand composite and bentonite. *J Water Process Eng*. 2016;14:86–100.
13. Hung DQ, Thanh NK. Preparation of NiFe₂O₄ - TiO₂ nanoparticles and study of their photocatalytic activity. *VNU J Sci Math Phys*. 2011;27:204–11.
14. Rahmayeni, Arief S, Stiadi Y, Rizal R, Zulhadjri. Synthesis of magnetic nanoparticles of TiO₂-NiFe₂O₄: characterization and photocatalytic activity on degradation of Rhodamine B. *Indones J Chem*. 2012;12:229–234.
15. Mohammadi M, Roknabadi MR, Behdani M, Kompany A. Enhancement of visible and UV light photocatalytic activity of rGO-TiO₂ nanocomposites: The effect of TiO₂/Graphene oxide weight ratio. *Ceram Int*. 2019;45:12625–34.
16. Mehrkhah R, Mohammadi M, Zenhari A, Baghayeri M, Roknabadi MR. Antibacterial evaporator based on wood-reduced graphene oxide/titanium oxide nanocomposite for long-term and highly efficient solar-driven wastewater treatment. *Ind Eng Chem Res*. 2023;62:4573–86.
17. Eramabadi P, Masoudi M, Makhdoumi A, Mashreghi M. Microbial cell lysate supernatant (CLS) alteration impact on platinum nanoparticles fabrication, characterization, antioxidant and antibacterial activity. *Mater Sci Eng C*. 2020;117:111292.
18. Bakhtiari-Sardari A, Mashreghi M, Eshghi H, Behnam-Rasouli F, Lashani E, Shahnavaz B. Comparative evaluation of silver nanoparticles biosynthesis by two cold-tolerant *Streptomyces* strains and their biological activities. *Biotechnol Lett*. 2020;42:1985–99.
19. Fan Y, Yang YN, Ding C. Preparation of g-C₃N₄/MoS₂ composite material and its visible light catalytic performance. *J Inorg Organomet P*. 2021;31:4722–30.
20. Younas M, Nadeem M, Atif M, Grossinger R. Metal-semiconductor transition in NiFe₂O₄ nanoparticles due to reverse cationic distribution by impedance spectroscopy. *J Appl Phys*. 2011;109:093704.
21. Amar VS, Puszynski JA, Shende RV. H₂ generation from thermochemical water-splitting using yttria stabilized NiFe₂O₄ core-shell nanoparticles. *J Renew Sustain Ener*. 2015;7:023113.
22. Jamsaz A, Goharshadi EK. Flame retardant, superhydrophobic, and superoleophilic reduced graphene oxide/orthoaminophenol polyurethane sponge for efficient oil/water separation. *J Mol Liq*. 2020;307:112979.
23. Linsebigler AL, Lu G, Yates JT, Jr. Photocatalysis on TiO₂ surfaces: principles, mechanisms, and selected results. *Chem Rev*. 1995;95:735–58.
24. Jandl S, Deslandes J. Infrared spectra of HFS₃. *Phys Rev B*. 1981;24:1040–4.
25. Basu S, Chatterjee S, Bhaumik A, Mukhopadhyay C. Ultrasound-promoted novel route to triazabenzobenzocyclopenta[*lm*]fluorenes: An efficient NiFe₂O₄@SiO₂-SO₃H nanocatalyst-assisted green synthesis. *Appl Organomet Chem*. 2021;35:e6426.
26. Naidu TM, Narayana PVL. Synthesis and characterization of Fe-TiO₂ and NiFe₂O₄ nanoparticles and its thermal properties. *J Nanosci Technol*. 2019;5:769–72.
27. Thy LTM, Linh NTC, Tram NTT, Tu TH, Tai LT, Khang PT, et al. Fabrication and response surface methodology for the adsorption of nickel ferrite-graphene oxide nanocomposite for the removal of methylene blue from water. *J Nanomater*. 2021;2021:4636531.
28. Wang X, Xie H, Wang Z, He K, Jing D. Graphene oxide as a multifunctional synergist of insecticides against lepidopteran insect. *Environ Sci Nano*. 2019;6:75–84.
29. Zhang Y, Qi F, Li Y, Zhou X, Sun H, Zhang W, et al. Graphene oxide quantum dot-sensitized porous titanium dioxide microspheres: Visible-light-driven photocatalyst based on energy band engineering. *J Colloid Interf Sci*. 2017;498:105–11.
30. Ciocarlan R-G, Seftel EM, Mertens M, Pui A, Mazaj M, Novak Tusar N, et al. Novel magnetic nanocomposites containing quaternary ferrites systems Co_{0.5}Zn_{0.25}Mn_{0.25}Fe₂O₄ (M = Ni, Cu, Mn, Mg) and TiO₂-anatase phase as photocatalysts for wastewater remediation under solar light irradiation. *Mater Sci Eng B Adv*. 2018;230:1–7.
31. Bao HV, Dat NM, Giang NTH, Thinh DB, Tai LT, Trinh DN, et al. Behavior of ZnO-doped TiO₂/rGO nanocomposite for water treatment enhancement. *Surf Interfaces*. 2021;23:100950.
32. Nguyen DCT, Cho KY, Oh WC. Synthesis of frost-like CuO combined graphene-TiO₂ by self-assembly method and its high photocatalytic performance. *Appl Surf Sci*. 2017;412:252–61.
33. Kim SR, Ali I, Kim JO. Phenol degradation using an anodized graphene-doped TiO₂ nanotube composite under visible light. *Appl Surf Sci*. 2019;477:71–8.
34. Liu L, Yue M, Lu J, Hu J, Liang Y, Cui W. The enrichment of photocatalysis via self-assembly perylene-tetracarboxylic acid diimide polymer nanostructures incorporating TiO₂ nano-particles. *Appl Surf Sci*. 2018;456:645–56.
35. Ebrahimzadeh Abrishami M, Mohammadi M, Sotoudeh M. Photocatalytic dye decomposition over CaMnO_{3-δ} and Pr_{0.5}Ca_{0.5}MnO₃: a combined XPS and DFT study. *Crystals*. 2022;12:1728.
36. Xiang Q, Yu J, Jaroniec M. Enhanced photocatalytic H₂-production activity of graphene-modified titania nanosheets. *Nanoscale*. 2011;3:3670–8.
37. Birhan D, Tekin D, Kiziltas H. Thermal, photocatalytic, and antibacterial properties of rGO/TiO₂/PVA and rGO/TiO₂/PEG composites. *Polym Bull*. 2022;79:2585–602.
38. Mann R, Mitsidis D, Xie Z, McNeilly O, Ng YH, Amal R, et al. Antibacterial activity of reduced graphene oxide. *J Nanomater*. 2021;2021:9941577.
39. Esther Nimshi R, Judith Vijaya J, Al-Najar B, Hazeem L, Bououdina M, John Kennedy L, et al. Multifunctional core-shell NiFe₂O₄ Shell with TiO₂/rGO nanostructures for biomedical and environmental applications. *Bioinorg Chem Appl*. 2022;2022:4805490.

Publisher's Note

Springer Nature remains neutral with regard to jurisdictional claims in published maps and institutional affiliations.